

## ELECTROCHEMICAL ENERGY

# Ultrahigh-current density anodes with interconnected Li metal reservoir through overlithiation of mesoporous $\text{AlF}_3$ framework

Hansen Wang,<sup>1</sup> Dingchang Lin,<sup>1</sup> Yayuan Liu,<sup>1</sup> Yuzhang Li,<sup>1</sup> Yi Cui<sup>1,2\*</sup>

Lithium (Li) metal is the ultimate solution for next-generation high-energy density batteries but is plagued from commercialization by infinite relative volume change, low Coulombic efficiency due to side reactions, and safety issues caused by dendrite growth. These hazardous issues are further aggravated under high current densities needed by the increasing demand for fast charging/discharging. We report a one-step fabricated  $\text{Li}/\text{Al}_4\text{Li}_9\text{-LiF}$  nanocomposite (LAFN) through an “overlithiation” process of a mesoporous  $\text{AlF}_3$  framework, which can simultaneously mitigate the abovementioned problems. Reaction-produced  $\text{Al}_4\text{Li}_9\text{-LiF}$  nanoparticles serve as the ideal skeleton for Li metal infusion, helping to achieve a near-zero volume change during stripping/plating and suppressed dendrite growth. As a result, the LAFN electrode is capable of working properly under an ultrahigh current density of  $20 \text{ mA cm}^{-2}$  in symmetric cells and manifests highly improved rate capability with increased Coulombic efficiency in full cells. The simple fabrication process and its remarkable electrochemical performances enable LAFN to be a promising anode candidate for next-generation lithium metal batteries.

## INTRODUCTION

The increasing demand from consumer electronics, electrical transportation, and grid-scale storage calls for higher energy density and lower-cost batteries (1, 2). Despite the great commercial success of lithium-ion (Li-ion) batteries, the current battery chemistries based on graphite anodes and transition metal oxide cathodes cannot meet the requirements in the long run (3). Li metal, with the highest theoretical capacity ( $3860 \text{ mA}\cdot\text{hour g}^{-1}$ ) and the lowest potential ( $-3.040 \text{ V}$  versus standard hydrogen electrode), is an attractive choice as the ultimate anode. Moreover, it is an indispensable component in the next-generation Li- $\text{O}_2$  and Li-S batteries (3–7). However, critical problems of Li metal anodes remain unsolved. Specifically, a Li metal anode does not have a host confining Li inside, causing marked dimension change during Li stripping/plating (8, 9). The fragile solid electrolyte interphase (SEI) cannot withstand the resulting mechanical deformation (10), such that it keeps breaking and repairing throughout cycling, leading to thick SEI and rapid capacity fading. Meanwhile, the cracks in SEI also locally concentrate the Li-ion flux, causing uncontrollable dendrite growth (11) and consequent safety issues. Under increased current densities for fast charging/discharging, accelerated volume fluctuation aggravates all the consequent hazardous issues, resulting in more severe battery failures.

Massive efforts have been made to solve the challenges of Li metal anodes, focusing on modifications of electrolytes (12–17), SEIs (8, 18–24), and separators (25–27). Meanwhile, elaborative engineering of the anode structure itself is also an important approach. Previous work includes use of Li powder instead of Li foil (10) and the fabrication of an exquisite current collector with rigorously designed structures for Li metal deposition (28–30). Although these different attempts effectively pushed forward Li metal anode engineering technique and alleviated certain aspects of the problems, few of them were able to simultaneously maintain a constant electrode volume and eliminate dendrite growth. Recently, we proposed

the concept of stable Li metal host, realized by embedding Li metal into hollow carbon spheres (31), the space between layers of graphene oxides (9), polymer fiber matrices (32), and macroporous structures (33, 34). These modifications successfully reduced volume change, suppressed dendrite growth, and achieved better cycle performance. However, these works are limited to current densities below  $5 \text{ mA cm}^{-2}$ . A higher working current density would cause capacity fading and instability of electrodes. Nevertheless, fast charging/discharging (current density greater than  $10 \text{ mA cm}^{-2}$ ) is indispensable for advanced batteries. Thus, it remains a formidable challenge to design a Li metal anode capable of operating under these high current densities.

To realize a normal operation under ultrahigh current densities, we believe that a Li metal anode would need to have the following properties: (i) an ultrastable host accommodating metallic Li to eliminate the damage on electrode and interfaces due to fast volume change during high-current density operation (essentially the whole electrode needs to have an almost zero volume fluctuation); (ii) a three-dimensional Li metal with a large electroactive surface area to effectively reduce the local current density; and (iii) an electrochemically inert, mechanically stable and highly Li-ion conducting interphase to protect the structure. Here, we developed a novel Li metal anode, which simultaneously has all the required properties. Using  $\text{Al}_4\text{Li}_9\text{-LiF}$  as a stable host, three-dimensional Li metal can be embedded into this nanocomposite ( $\text{Li}/\text{Al}_4\text{Li}_9\text{-LiF}$ ) (LAFN) through a simple one-step “overlithiation” process of mesoporous  $\text{AlF}_3$ . We demonstrated that LAFN is an ideal host with near-zero volume change during stripping/plating. In addition, despite the space occupied by the skeleton, the metallic Li in the LAFN composite still offered a high specific capacity of  $\sim 1571 \text{ mA}\cdot\text{hour g}^{-1}$  and a volumetric capacity of  $\sim 1447 \text{ mA}\cdot\text{hour cm}^{-3}$ . Meanwhile, LiF formed during overlithiation serves as a protective material both electrochemically and mechanically to improve the stability of the Li metal anode. Moreover, it also promotes the homogeneity of Li-ion diffusion, which can effectively suppress dendrite growth. Because of these superiorities, an LAFN anode is capable of achieving a long cycle life with low overpotential and high capacity and is able to work stably under an unprecedented high current density of  $20 \text{ mA cm}^{-2}$  for at least 100 cycles.

<sup>1</sup>Department of Materials Science and Engineering, Stanford University, Stanford, CA 94305, USA. <sup>2</sup>Stanford Institute for Materials and Energy Sciences, SLAC National Accelerator Laboratory, 2575 Sand Hill Road, Menlo Park, CA 94025, USA.

\*Corresponding author. Email: yicui@stanford.edu

Copyright © 2017  
The Authors, some  
rights reserved;  
exclusive licensee  
American Association  
for the Advancement  
of Science. No claim to  
original U.S. Government  
Works. Distributed  
under a Creative  
Commons Attribution  
NonCommercial  
License 4.0 (CC BY-NC).

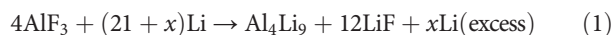
Downloaded from <http://advances.sciencemag.org/> on September 11, 2017

## RESULTS

## Fabrication and morphology of LAFN

Synthesis of LAFN starts from Li metal foil and  $\text{AlF}_3$  powder. Figure 1 (D to F) shows the scanning electron microscopy (SEM) morphology of the pristine  $\text{AlF}_3$  powder. It is composed of secondary particles with a diameter of  $\sim 20 \mu\text{m}$  (Fig. 1D). Each particle consists of layers of columnar  $\text{AlF}_3$  arrays (Fig. 1, A, E, and F). These  $\text{AlF}_3$  arrays, with a column diameter of  $\sim 40 \text{ nm}$  and spacing of  $\sim 20 \text{ nm}$ , provide a mesoporous framework for Li reaction and infusion, making the  $\text{AlF}_3$  an ideal precursor for overlithiation. Hysteresis on the  $\text{N}_2$  adsorption-desorption isotherm of  $\text{AlF}_3$  powder (fig. S1) further proves the mesoporous structure. Overlithiation of this mesoporous  $\text{AlF}_3$  framework follows reaction 1, where the alloy product is reasonably deduced through a Li-Al phase diagram (35). Existence of the products will be further proven through x-ray diffraction (XRD) characterization below. As shown in the equation, overstoichiometric Li metal reacts with mesoporous  $\text{AlF}_3$  framework. In this way, stoichiometric Li metal is able to react with  $\text{AlF}_3$ , directly participating into the framework construction, whereas excess Li metal fills into the interspace of this framework. According to the reaction equation, mass ratio between  $\text{AlF}_3$  and Li in a stoichiometric reaction should be 0.4:0.17 g. Our overlithiation reaction used an overstoichiometric Li of 0.4:0.37 g.

Theoretically, this ratio would give a final capacity of  $1003 \text{ mA-hour g}^{-1}$  coming from the excess Li metal embedded inside.



After putting  $\text{AlF}_3$  and Li foil into a crucible, an elevated temperature of  $\sim 350^\circ\text{C}$  and continuous stirring were applied. After Li metal melted, it could be separated into small droplets among the white powder of  $\text{AlF}_3$  (fig. S2A). This phenomenon indicated the lithiophilic feature of the mesoporous  $\text{AlF}_3$  framework; otherwise, lithium would become a large droplet to reduce surface area. With continuous stirring, smaller and smaller Li droplets were observed, whereas the color of  $\text{AlF}_3$  powder gradually turned from white to gray and then to black (fig. S2, B and C), indicating the formation of an  $\text{Al}_4\text{Li}_9$ -LiF skeleton (Fig. 1B). After a proper time of stirring, the remaining tiny lithium droplets would permeate into the black powder of the  $\text{Al}_4\text{Li}_9$ -LiF skeleton, suggesting the infusion of excess lithium into the framework (Fig. 1C). After the reaction, black powders of various sizes were obtained (fig. S2D). Later on, LAFN powders were size-selected to remove very large particles (fig. S2E) and mechanically pressed into electrodes (fig. S2F). Electrode thickness could be controlled for various electrochemical testing. The pore spaces

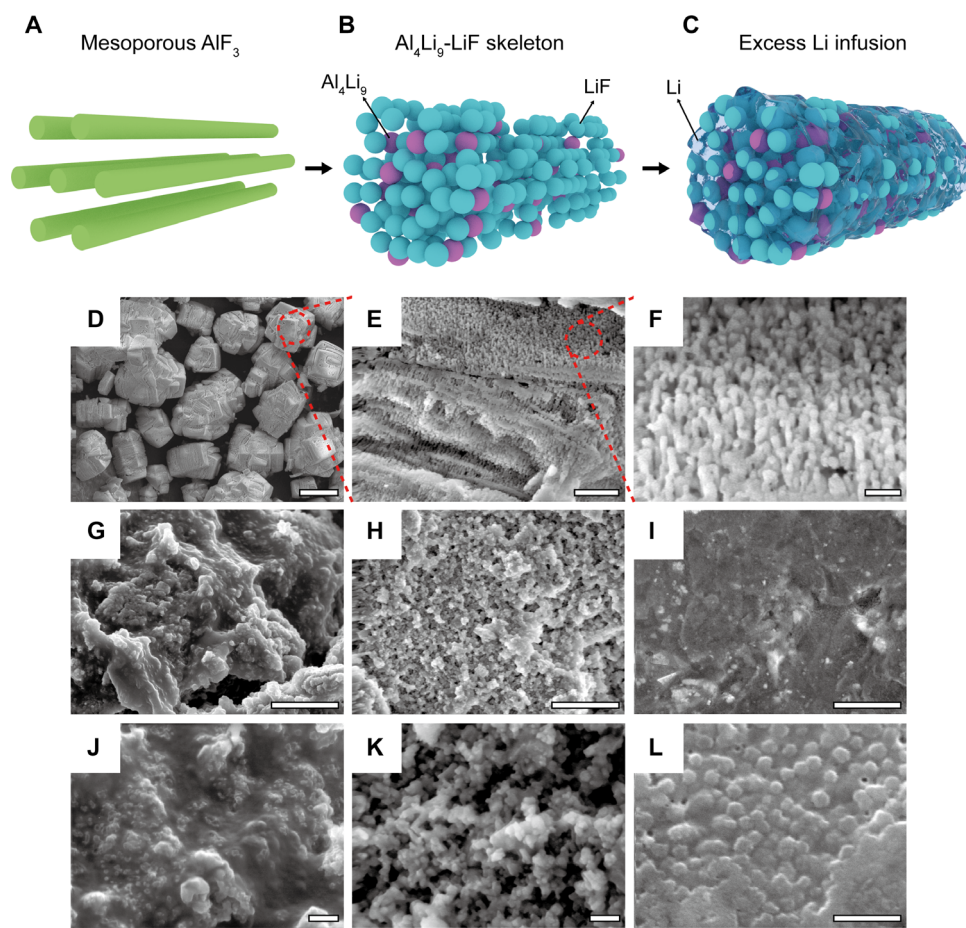


**Fig. 1. Morphology of  $\text{AlF}_3$  powder and LAFN.** (A) Sketch of  $\text{AlF}_3$  powder mesoporous framework. (B) Sketch of  $\text{Al}_4\text{Li}_9$ -LiF skeleton. (C) Sketch of LAFN. (D to F) SEM images of  $\text{AlF}_3$  powder under different magnifications. Scale bars,  $20 \mu\text{m}$  (D),  $1 \mu\text{m}$  (E), and  $200 \text{ nm}$  (F). (G to I) SEM images of pristine LAFN surface, LAFN surface after stripping  $5 \text{ mA-hour cm}^{-2}$  of Li metal, and LAFN surface after stripping and plating back  $5 \text{ mA-hour cm}^{-2}$  of Li metal. Scale bars,  $2 \mu\text{m}$ . (J to L) Magnified SEM images of (G) to (I). Scale bars,  $200 \text{ nm}$ .

between LAFN secondary particles were still maintained, and the electrolyte was found to be very compatible with LAFN electrode (fig. S3). As a result, Li ions can be transferred into the framework and used wherever needed during cycling.

Figure 1 (G and J) shows the SEM images of LAFN powder under different magnifications. After the overlithiation process, the columnar arrays of pristine  $\text{AlF}_3$  were converted into particles about 50 to 100 nm in diameter because of the reaction with Li metal. Meanwhile, the porous structure was maintained after the reaction, with excess Li metal infused into the host skeleton. Figure S4A shows a transmission electron microscopy image of a LAFN secondary particle. It can be observed that the secondary particle is composed of numerous small particles, in accordance with the SEM morphology. Energy-dispersive x-ray spectroscopy (EDX) mapping was done for Al and F (fig. S4, B to D). Al tends to concentrate in the center of the particle, whereas F spreads out in the whole area, especially on the surface of the particle. Note that the sporadic Al element observed in the outer part of the particle can be attributed to the unreacted  $\text{AlF}_3$ . Figure 1 (H and K) shows the SEM images of LAFN morphology after stripping 5 mA-hour  $\text{cm}^{-2}$  of metallic Li. The porous skeleton formed by  $\text{Al}_4\text{Li}_9$ -LiF nanoparticles could be obviously observed after Li stripping on the surface. After plating back 5 mA-hour  $\text{cm}^{-2}$  of Li, most of the metallic Li deposited back into the porous structure, with  $\text{Al}_4\text{Li}_9$ -LiF nanoparticles faintly visible underneath (Fig. 1, I and L). This  $\text{Al}_4\text{Li}_9$ -LiF nanoparticle framework with Li metal infusion structure can be further exhibited through sketch in Fig. 1C, in which the blue nanospheres represent the as-formed LiF nanoparticles, and the purple nanospheres represent the  $\text{Al}_4\text{Li}_9$  nanoparticles. These nanoparticles stack up to form a skeleton with interconnected pathways, filled with excess metallic Li (transparent). From the reaction stoichiometry, we know that the ratio of Al to F should be 1:3, reasonably indicating a much larger amount of LiF particles than  $\text{Al}_4\text{Li}_9$ . In addition, this is also in accordance with the abovementioned EDX result, where  $\text{Al}_4\text{Li}_9$  mostly concentrates in the center of secondary particles and is surrounded by LiF nanoparticles. This structure will be further proven later.

### Li dendrite suppression and near-zero volume change

Morphologies of Li foil and LAFN after different symmetric cell cycles and current densities in carbonate-based electrolyte (see Materials and Methods) were observed. After one cycle of Li stripping and plating under a current density of 1 mA  $\text{cm}^{-2}$  and a capacity of 1 mA-hour  $\text{cm}^{-2}$ , the Li foil surface was covered with numerous dendrites, tangling with each other (Fig. 2B). Meanwhile for the LAFN electrode, a smooth surface was maintained because of the confining effect and the homogeneous growth among the framework (Fig. 2C). Low-magnification SEM images can be seen in fig. S5 (A and B). After 10 cycles under a current density of 1 mA  $\text{cm}^{-2}$  and a capacity of 1 mA-hour  $\text{cm}^{-2}$ , the dendrite on the Li foil surface became much thinner, which could increase the possibility of piercing the separator, causing a soft short circuit (fig. S6, A and C). However, for the LAFN electrode, no dendrite growth was observed on the surface (fig. S6, B and D). Even when we increased the applied current density to 20 mA  $\text{cm}^{-2}$ , with capacity fixed at 1 mA-hour  $\text{cm}^{-2}$ , the LAFN electrode showed no Li metal dendrites (Fig. 2E) after one cycle of stripping and plating, whereas the dendrites formed on Li foil surface curled up because of the increased heterogeneity under higher current density (Fig. 2D). Low-magnification SEM images can be seen in fig. S5 (C and D). In addition, fig. S7 shows the morphology of LAFN electrodes after 50 and 100 cycles under a current density of 1 mA  $\text{cm}^{-2}$  and a capacity of 1 mA-hour  $\text{cm}^{-2}$ ,

and fig. S8 shows that of LAFN electrodes after 10 and 30 cycles under a current density of 1 mA  $\text{cm}^{-2}$  and a capacity of 3 mA-hour  $\text{cm}^{-2}$ . Both figures further prove the exciting capability of LAFN electrodes to suppress dendrite growth even after long cycling. Furthermore, fig. S9 shows the morphology of LAFN electrode (without any prestripping) after directly plating 1 mA-hour  $\text{cm}^{-2}$  and 5 mA-hour  $\text{cm}^{-2}$  of Li metal onto it. From the uniform surface of these electrodes, we can conclude that LAFN electrodes did not only offer a skeleton for Li metal but also modified interface chemistry for Li metal plating homogeneity.

Dendrite growth is successfully suppressed owing to three vital factors. The distinctive skeleton of  $\text{Al}_4\text{Li}_9$  surrounded by LiF nanoparticles plays a very important role. As shown in Fig. 2A, if we have a very conductive skeleton, electrons can efficiently transfer to the anode surface, and then the Li metal will be plated back onto the surface of this electrode because of the high availability of both electrons and ions, leaving the skeleton reservoir empty. Dendrite growth will also be promoted because of the uneven surface and locally concentrated Li-ion flux. However, for LAFN, the insulating LiF nanoparticles (blue) dominate the skeleton and hold  $\text{Al}_4\text{Li}_9$  (purple) inside (Fig. 2A), effectively restraining the electron transfer to the surface. In this case, the framework is not very conductive. This promotes Li metal to be plated back inside the structure onto the underlying reserved Li, where electrons are available, gradually filling the whole skeleton. Then, dendrite growth can be suppressed to a great extent because all stripped Li metals are used to fill the skeleton again, and the nanocomposite structure can be effectively maintained during recurrent cycles. Besides, the effect of LiF itself suppressing dendrite growth has also been previously reported and proven (36–41). Li halide salts are capable of reducing the activation energy barrier for Li-ion diffusion at an electrode/electrolyte interface (14, 42). This increased Li-ion diffusivity further promotes Li ion to transfer inside the skeleton and plate onto existing Li metal instead of growing into dendrites on the surface. In addition, for Li foil, only surface Li has access to electrolyte and Li cations, whereas LAFN reduces the effective local current density and the Li cation flux around the nuclei due to the increased surface area, thus increasing the deposition homogeneity.

Volume stability of LAFN was also characterized through thickness testing of electrodes after stripping and plating metallic Li. LAFN was pressed into the electrode, the cross-sectional image of which is shown in Fig. 2F. We made an ultrathick electrode of about 760  $\mu\text{m}$ , aiming at increasing the volume change effect for better observation. Figure 2G shows the cross-sectional image of an LAFN electrode after stripping 37.5 mA-hour  $\text{cm}^{-2}$  of Li metal inside (equivalent to  $\sim 181.93$ - $\mu\text{m}$ -thick Li foil). The thickness shrinkage was only  $\sim 10$   $\mu\text{m}$  ( $\sim 1.3\%$  change). Essentially, the volume change was near zero, indicating that the electrode is capable of maintaining the skeleton structure after Li metal stripping. Later, 37.5 mA-hour  $\text{cm}^{-2}$  of Li metal was plated back, and Fig. 2H shows that the electrode maintained a thickness of  $\sim 760$   $\mu\text{m}$  very well. To guarantee the accuracy of this experiment, all three samples were cut from the same piece of LAFN electrode. The near-zero volume change of LAFN is remarkable, for it not only indicates that LAFN successfully provides a stable interconnected reservoir for Li metal for effective stripping and plating but also further confirms the capability of Li metal plating back into the skeleton instead of growing on the electrode surface, guaranteeing the structure reusability during later cycling. Compared with the previous work of graphene oxide host with  $\sim 20\%$  volume change (9) and polymer fiber matrix with 2.4% volume change (32), the near-zero volume change here is very significant and will serve as a crucial factor for the cycling stability under ultrahigh current densities.

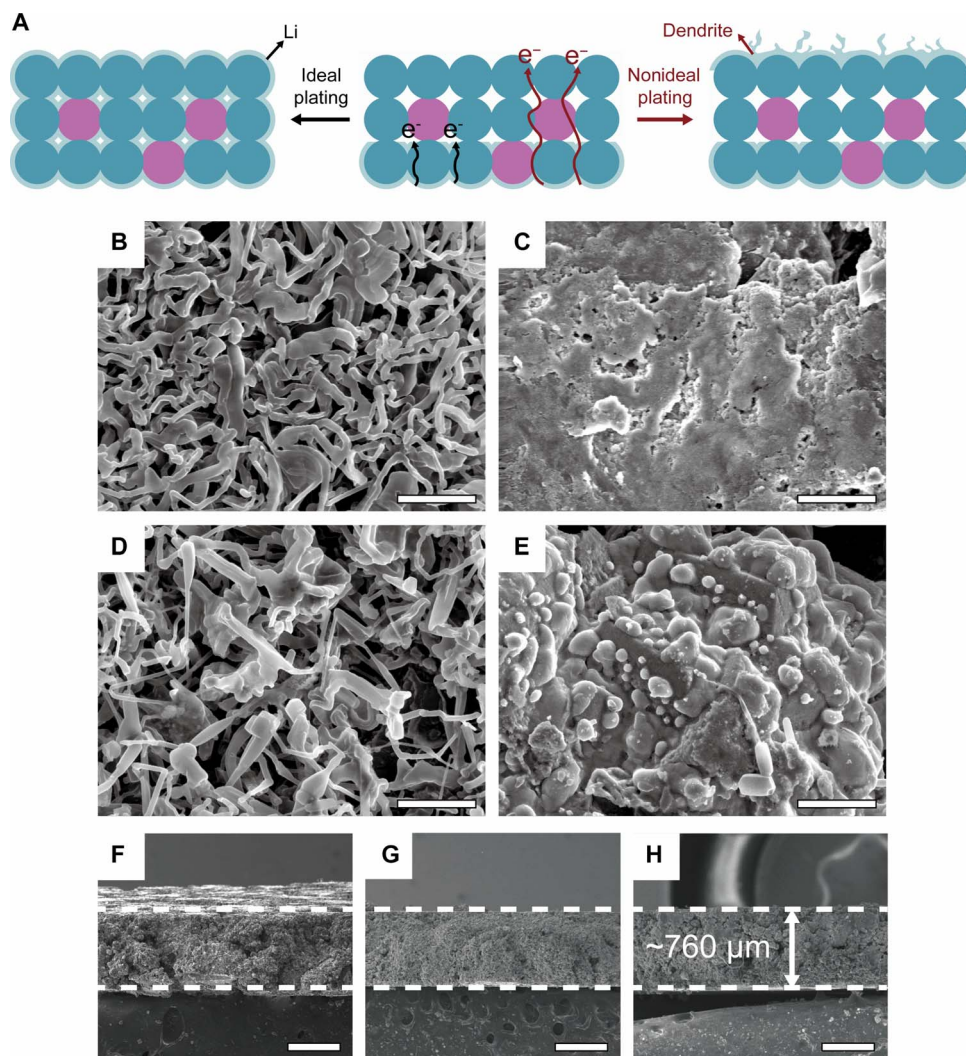


**Fig. 2. Dendrite-suppressed, volume-stable LAFN electrode.** (A) Sketch of ideal and nonideal plating processes due to different conductivities of the skeleton. (B and C) SEM images of Li foil surface (B) and LAFN surface (C) after one symmetric cell cycle under  $1 \text{ mA cm}^{-2}$  and  $1 \text{ mA-hour cm}^{-2}$ . Scale bars,  $5 \mu\text{m}$ . (D and E) SEM images of Li foil surface (D) and LAFN surface (E) after one symmetric cell cycle under  $20 \text{ mA cm}^{-2}$  and  $1 \text{ mA-hour cm}^{-2}$ . Scale bars,  $5 \mu\text{m}$ . (F to H) Cross-sectional SEM images of a pristine LAFN electrode (F), an LAFN electrode after stripping  $37.5 \text{ mA-hour cm}^{-2}$  of Li (G), and an electrode after stripping and plating back  $37.5 \text{ mA-hour cm}^{-2}$  of Li (H). Scale bars,  $500 \mu\text{m}$ .

### LiF-protected skeleton with Li-ion conductivity

Basic electrochemical properties were further characterized for LAFN. Electrochemical impedance spectroscopy (EIS) was tested for as-assembled symmetric cells. Figure 3A shows the Nyquist plot for LAFN symmetric cells for the first 20 hours, and Fig. 3B shows that for Li foil. The high-frequency semicircles are good indicators of the charge transfer resistance on the electrode-electrolyte interfaces. Because of the unavoidable native oxide layer, Li foil showed an extremely high interfacial resistance of  $\sim 1600 \text{ ohms}$ , whereas for LAFN, a highly reduced resistance of  $\sim 8 \text{ ohms}$  could be observed. Impedance performances were also tested after cycling of LAFN and Li foil symmetric cells (fig. S10). For Li foil, the charge transfer resistance rapidly decreased to  $\sim 35 \text{ ohms}$  mainly because of the broken native oxide layers as well as largely increased surface area caused by dendrite growth. Meanwhile, LAFN showed a rather stable and consistently low resistance even after 100 cycles. This low interfacial resistance offers

a further improved charge transfer capability compared to graphene oxide ( $\sim 30 \text{ ohms}$ ) (9). For Li foil, in contrast, continuous side reactions happen because of the exposure of Li to electrolyte, and the accumulated SEI layer with poor Li-ion conductivity leads to high resistance. These results guarantee that Li metal inside LAFN can be cycled with lower driving force for charge transferring. Furthermore, after stripping Li metal from one electrode to the other, charge transfer resistance of LAFN symmetric cells increased very slightly (fig. S11). Even when 50% of the capacity (up to  $30 \text{ mA-hour cm}^{-2}$ ) was stripped from one electrode, the charge transfer resistance only increased from  $\sim 8$  to  $\sim 13 \text{ ohms}$ . This further indicates the stable interface properties of LAFN during cycling due to its interconnected matrix.

Although an  $\text{Al}_4\text{Li}_9$ -LiF skeleton occupied a large part of the nanocomposite, a high specific capacity could still be retained. After stripping Li metal inside LAFN electrode to  $1 \text{ V}$  versus  $\text{Li}^+/\text{Li}$  under a very low current density of  $\sim 0.2 \text{ mA cm}^{-2}$ , the voltage profile (Fig. 3C) showed

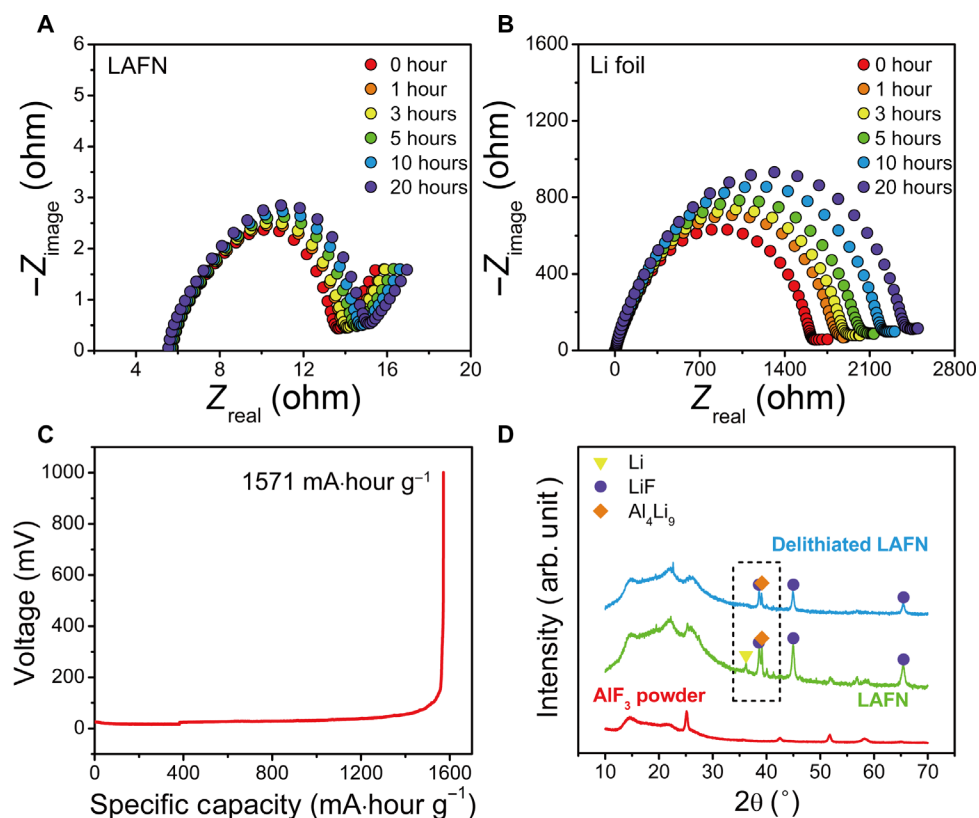


**Fig. 3. Electrochemical properties of LAFN electrode.** (A and B) Impedance performance of LAFN electrode (A) and Li foil electrode (B). (C) Voltage profile of stripping Li from LAFN electrode to 1 V versus  $\text{Li}^+/\text{Li}$ . (D) XRD characterization of LAFN electrode before and after stripping Li to 1 V versus  $\text{Li}^+/\text{Li}$ . arb. unit, arbitrary unit.

a total specific capacity of  $1571 \text{ mA}\cdot\text{hour g}^{-1}$ . No second plateau can be observed, indicating that only excess Li metal contributed to this capacity. This result is even higher than the theoretical capacity of excess Li metal ( $1003 \text{ mA}\cdot\text{hour g}^{-1}$ ), which can be attributed to the incomplete reaction between  $\text{AlF}_3$  and Li. XRD was also applied to confirm this. In Fig. 3D, the green curve of pristine LAFN confirms the formation of  $\text{Al}_4\text{Li}_9$ -LiF framework and the existence of excess Li metal as well as  $\text{AlF}_3$  that have not completely reacted with Li metal (small peaks between  $50^\circ$  and  $60^\circ$ ). In addition, the blue curve shows the sample structure after stripping Li metal to 1 V versus  $\text{Li}^+/\text{Li}$ . The amorphous halo on the left side of these curves can be attributed to the Kapton tape for sealing. Compared to pristine LAFN, delithiated sample no longer had a Li peak, while still maintaining a high  $\text{Al}_4\text{Li}_9$  peak. This feature can be observed more easily in a magnified figure (fig. S12), in accordance with the delithiation voltage profile with no second plateau. X-ray photoelectron spectroscopy (XPS) was also applied for pristine LAFN and delithiated LAFN to further confirm its structure (fig. S13). The lack of Al peaks on the surface of both pristine and fully stripped samples proves that  $\text{Al}_4\text{Li}_9$  alloy is in good protection of LiF nanoparticles. After delithiation, metal Li peak also disappeared, confirming the full stripping of excess Li metal. From these results, we may reasonably deduce that all excess Li was used during the delithiation process, and the  $\text{Al}_4\text{Li}_9$  framework was protected in good condition, possibly because of the protection of electronically insulating LiF nanoparticles. The insulating LiF confined  $\text{Al}_4\text{Li}_9$  particles inside to maintain a stable skeleton while still offered an excellent interconnected pathway for Li metal and Li ions. This feature further revealed the superiority of overlithiation as well as the potential remarkable performance of LAFN battery systems.

### Electrochemical performance of LAFN

Here, galvanostatic symmetric cell cycle capability was first compared between Li foil and LAFN. Figure S14 shows the voltage profile of Li foil and LAFN symmetric cells during the 1st, 10th, 50th, and 100th cycles, with current density fixed at  $1 \text{ mA cm}^{-2}$  and capacity fixed at  $1 \text{ mA}\cdot\text{hour cm}^{-2}$  in carbonate-based electrolytes. For the Li foil symmetric cell, high overpotential could be seen at the beginning of charging process during the first cycle, owing to the preobserved poor ionic conductivity of SEI on Li surface. High overpotential was also observed at the beginning and end of discharging process, corresponding to the increased difficulty of Li nucleation beneath thick SEI and the usage of previously unused fresh Li beneath the surface, respectively. This effect faded with cycle number, because of the broken SEI layer on the surface of Li foil and the increased real surface area after dendrite growth. On the contrary, LAFN showed flat, smooth voltage plateaus during charging and discharging processes with a low overpotential below 40 mV, as well as better stability after 100 cycles. This superiority can be further proven in Fig. 4A, where LAFN symmetric cells offered a consistent, stable low overpotential about 35 mV during the first 100 cycles, much lower than that of Li foil counterparts, whose overpotential fluctuated between 60 and 160 mV. Actually, long-term cycle capability was also tested, and the result can be seen in fig. S15A. LAFN maintained stable cycling after 500 hours of testing, corresponding to 250 cycles, which could be seen from the enlarged figures from the 90th to 100th cycles (fig. S15B) and 230th to 240th cycles (fig. S15C). Although the overpotential increased from  $\sim 35$  to  $\sim 45$  mV, stable charging and discharging plateaus were maintained. Meanwhile for Li foil, marked overpotential increase could be seen after 250 hours.

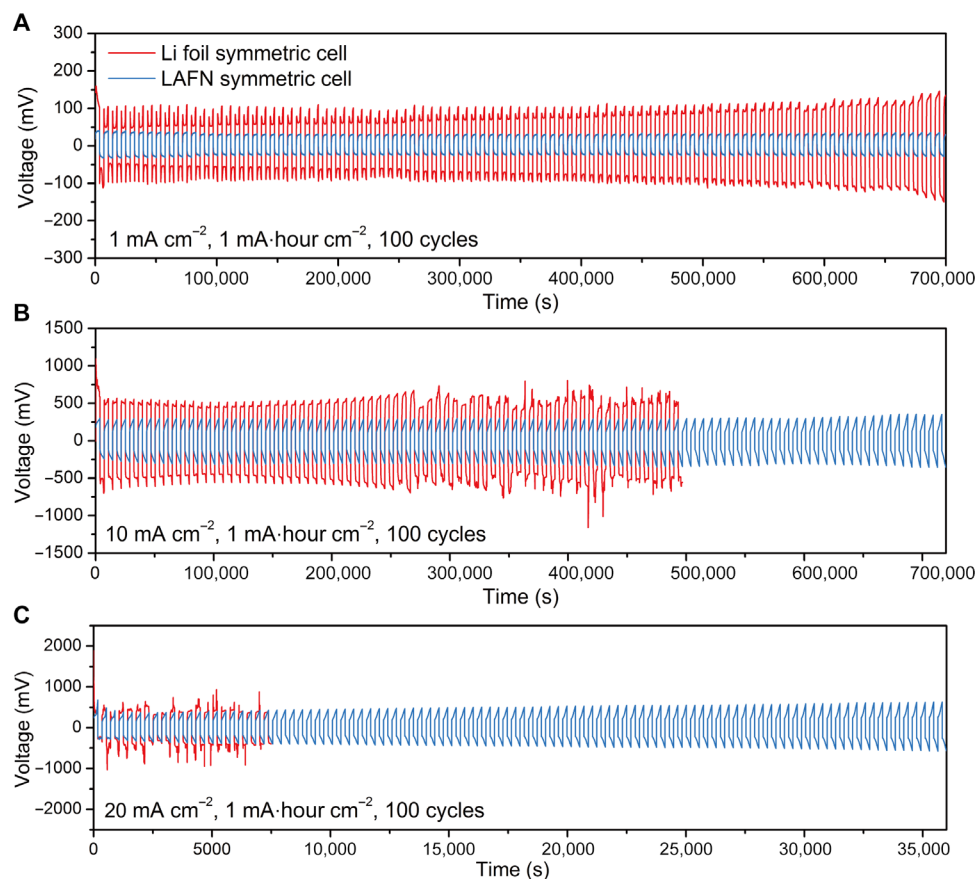


**Fig. 4. Symmetric cell cycling performance of LAFN.** (A to C) Symmetric cell cycling performance comparison between Li foil (red) and LAFN (blue) under  $1 \text{ mA cm}^{-2}$  (A),  $10 \text{ mA cm}^{-2}$  (B), and  $20 \text{ mA cm}^{-2}$  (C). Areal capacity was fixed at  $1 \text{ mA}\cdot\text{hour cm}^{-2}$ .

Later, cycling tests were carried out under increased current densities of  $3 \text{ mA cm}^{-2}$  (fig. S16),  $5 \text{ mA cm}^{-2}$  (fig. S17),  $10 \text{ mA cm}^{-2}$  (Fig. 4B), and  $20 \text{ mA cm}^{-2}$  (Fig. 4C), with capacity fixed at  $1 \text{ mA}\cdot\text{hour cm}^{-2}$ . The overpotential of LAFN increased from  $75 \text{ mV}$  under  $3 \text{ mA cm}^{-2}$ ,  $150 \text{ mV}$  under  $5 \text{ mA cm}^{-2}$ , to  $240 \text{ mV}$  under  $10 \text{ mA cm}^{-2}$ , and then to  $400 \text{ mV}$  under  $20 \text{ mA cm}^{-2}$ . Meanwhile, stable, smooth cycling plateaus were maintained for the first 100 cycles. In contrast, the Li foil symmetric cell showed not only much higher overpotential but also marked fluctuation during charging and discharging processes. To be more specific, cycling plateaus during different time periods under various current densities are directly plotted for a better comparison (fig. S18). It can be easily observed that the interconnected lithium reservoir and faster kinetics of LAFN not only enabled it to work under much mitigated hysteresis, but also kept flat and smooth cycling plateaus without fluctuations caused by local heterogeneity or soft short circuit. It should be noted that  $20 \text{ mA cm}^{-2}$  is an unprecedented high current density that has rarely been used, if any, in the tests of Li metal anodes. For Li foil symmetric cells under  $20 \text{ mA cm}^{-2}$ , a high overpotential of  $\sim 2 \text{ V}$  was observed at the beginning of the first cycle (fig. S19), followed by a drop to a level even lower than that under  $10 \text{ mA cm}^{-2}$ , indicating a soft short circuit within the cells. In contrast, LAFN was capable of working stably under such a high current density for the first 100 cycles, with suppressed dendrite growth (Fig. 2E), verifying the potential of maintaining a stable interface and cycling performance under high current densities. In fig. S20, the voltage profile comparison is shown between LAFN and Li foil symmetric cell cycling under metabolic current

densities from  $0.5$  to  $10 \text{ mA cm}^{-2}$  and back to  $0.5 \text{ mA cm}^{-2}$ , with capacity fixed at  $1 \text{ mA}\cdot\text{hour cm}^{-2}$ . Continuous flat charging and discharging plateaus with obvious lower overpotential can be seen under all applied current densities for LAFN, manifesting its capability of working under mutative current densities for varied purposes. In addition, cycling performance under a current density of  $1 \text{ mA cm}^{-2}$ , with areal capacity corresponding to that of a commercial battery ( $3 \text{ mA}\cdot\text{hour cm}^{-2}$ ), was also tested (fig. S21). Li foil symmetric cells showed a high overpotential at the end of charging and discharging processes and stopped working after about 35 cycles. In comparison, LAFN symmetric cells worked normally after over 400 hours (more than 70 cycles), with stable and low voltage plateaus in each cycle, manifesting potential of commercial level cycle capability.

All these superiorities were further validated through full cell testing. Full cells using LAFN or Li foil paired with a  $\text{LiCoO}_2$  (LCO) cathode were compared through rate capability tests. Higher capacity was constantly retained using LAFN as an anode, especially at higher rates. Here, we used an LCO cathode with an active material mass of  $\sim 3.6 \text{ mg}$ . Using a theoretical specific capacity of  $140 \text{ mA}\cdot\text{hour g}^{-1}$ , we can calculate that a rate of  $1 \text{ C}$  corresponds to a current density of  $0.5 \text{ mA cm}^{-2}$ . The LCO/Li foil full cell only offered capacities of  $125 \text{ mA}\cdot\text{hour g}^{-1}$  under  $0.2 \text{ C}$ ,  $100 \text{ mA}\cdot\text{hour g}^{-1}$  under  $1 \text{ C}$ ,  $73 \text{ mA}\cdot\text{hour g}^{-1}$  under  $4 \text{ C}$ , and  $5 \text{ mA}\cdot\text{hour g}^{-1}$  under  $10 \text{ C}$ . In comparison, the LCO/LAFN full cell gave capacities of  $140 \text{ mA}\cdot\text{hour g}^{-1}$  under  $0.2 \text{ C}$ ,  $131 \text{ mA}\cdot\text{hour g}^{-1}$  under  $1 \text{ C}$ ,  $113 \text{ mA}\cdot\text{hour g}^{-1}$  under  $4 \text{ C}$ , and  $\sim 80 \text{ mA}\cdot\text{hour g}^{-1}$  under  $10 \text{ C}$  (Fig. 5A). Here, all specific capacities were calculated on the

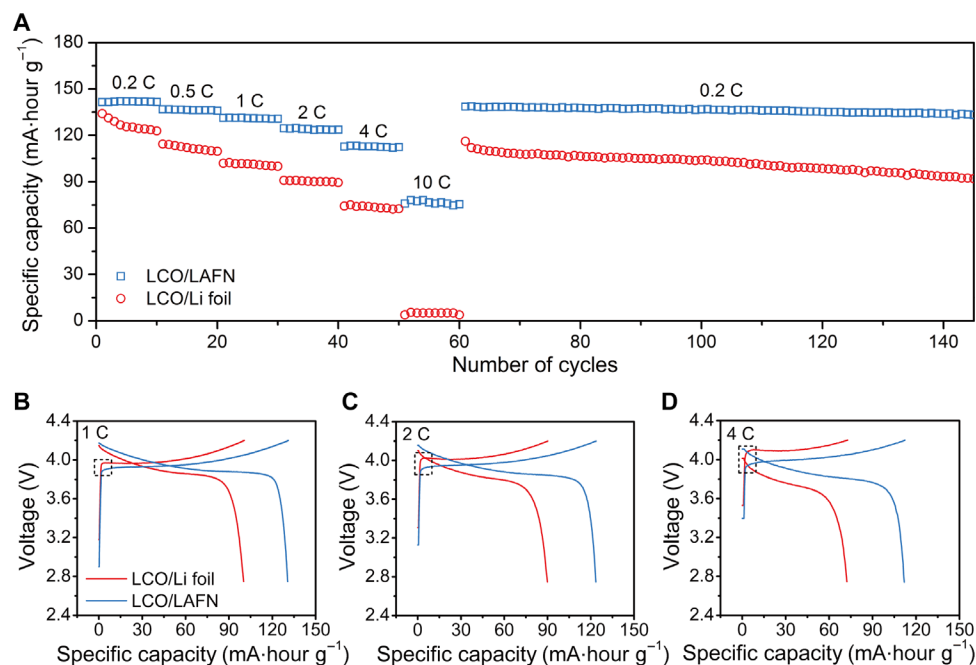


**Fig. 5. Electrochemical performance of LCO/LAFN cells.** (A) Rate capability of LCO/LAFN cells and LCO/Li foil cells at various rates from 0.2 to 10 C. (B to D) Voltage profile comparison between LCO/LAFN cells and LCO/Li foil cells at rates of 1 C (B), 2 C (C), and 4 C (D). The dotted boxes are enlarged in fig. S23 (A to C).

basis of active LCO mass. LAFN can work properly under high rates, under which Li foil has already failed, further confirming the capability of LAFN working under high current densities. It should be noted that the capacity of the LCO/LAFN full cell also showed much better stability than that of LCO/Li foil full cell. The capacity of the LCO/LAFN full cell under a high rate of 10 C showed little fluctuation during the 10 cycles tested, with no trend of fading. Moreover, after resetting the rate to 0.2 C, the LCO/LAFN full cell maintained the original capacity and was very stable during the following 90 cycles, whereas the capacity of the LCO/Li foil full cell after resetting the rate back to 0.2 C was lower than that of the first cycle and kept decaying for the next 90 cycles. Cycling stability was also tested under 1 C with five cycles under 0.2 C for electrode activation (fig. S22), and higher capacity with better stability can still be observed for LAFN. These results in full cells may be related to the reduced hysteresis using LAFN as an anode. Higher overpotential could be observed for a Li foil anode at the beginning of each charging plateau (Fig. 5, B to D, dotted box, and fig. S23, A to C), owing to the sluggish kinetics at Li foil/electrolyte interface. This effect is also in accordance with symmetric cell cycling voltage profiles. As we increased the rate, this hysteresis effect was also boosted (fig. S24, A to C), corresponding to the enhanced capacity gap between LCO/Li foil and LCO/LAFN full cells. The remarkable performance of the LAFN anode with the LCO cathode further verifies its potential as industrialized Li metal anode material.

LAFN and Li foil were also paired with high-areal capacity  $\text{Li}_4\text{Ti}_5\text{O}_{12}$  (LTO;  $\sim 3.3 \text{ mA}\cdot\text{hour cm}^{-2}$ ). LTO/LAFN cells still showed a highly increased rate capacity than LTO/Li foil cells, especially under higher rates (fig. S25A). To be noted, here, a rate of 3 C corresponds to a current density as high as  $10 \text{ mA cm}^{-2}$ . Thus, the capability of LAFN working under high current densities is further verified. LAFN also showed highly reduced hysteresis during full cell cycling, in accordance with LCO full cell results (fig. S25, B to E). Meanwhile, the most important role of the high-areal capacity LTO cells was to serve as an indirect indicator of Coulombic efficiency (CE) of the anodes. LTO itself

does not provide Li during cycling, only serving as a Li reservoir. Moreover, the CE of LTO is near 100% except at initial cycles. As a result, only anodes serve as Li sources, and the loss of Li can be mostly attributed to the low CE of the anodes. We paired the high-areal capacity LTO electrode with 50- $\mu\text{m}$ -thick Li metal foil ( $\sim 10 \text{ mA}\cdot\text{hour cm}^{-2}$ ) and LAFN electrode with a capacity of  $\sim 16 \text{ mA}\cdot\text{hour cm}^{-2}$  (thinnest electrode can be fabricated using LAFN powder) and tested their cycle life under 0.5 C. The point where specific capacity begins to fade markedly indicates the cycle number used to consume excess Li metal in LAFN or Li foil. As shown in fig. S26, capacity of LTO/Li foil cell started to fade at the 28th cycle, illustrating a CE of  $\sim 92.7\%$ . In contrast, the capacity of LTO/LAFN cell remained almost constant even after 150 cycles, giving a CE of at least  $\sim 97.4\%$ , showing further improvements even compared to previously reported polymer fiber matrix (32).

## DISCUSSION

LAFN as a Li metal anode was synthesized through the overlithiation process of a mesoporous  $\text{AlF}_3$  framework. LAFN had a porous skeleton with an interconnected Li metal reservoir. This designing not only offered a stable host for lithium metal during stripping and plating but also took advantage of the reaction-produced insulating  $\text{LiF}$  for the electrochemical protection of the  $\text{Al}_4\text{Li}_9$  nanoparticles as well as Li cation diffusion promoter for increased Li metal plating homogeneity. These superiorities endowed LAFN with suppressed dendrite growth and near-zero volume change. As a result, LAFN showed much stable charging and discharging plateaus in symmetric cells, much higher capacity capability in full cells using LCO/LTO cathodes, and increased CE, compared to Li foil. The LAFN anode worked properly under an unprecedented high current density of  $20 \text{ mA cm}^{-2}$ , under which Li foil shorted immediately. Considering the safe and single-step fabrication procedure, we believe that LAFN may inspire designs of next-generation Li metal anode that can accommodate fast charging/discharging demands in the near future.

## MATERIALS AND METHODS

## LAFN fabrication

AlF<sub>3</sub> powder (Aldrich) was transferred into an argon-filled glove box with sub-parts per million O<sub>2</sub> level for later use. AlF<sub>3</sub> powder (0.40 g) was firstly put into a stainless steel crucible on a hot plate heated up to ~350°C. Afterward, 0.37 g of Li foil (99.9%; Alfa Aesar) was weighted, cut into small pieces, and put into the crucible. Excess lithium foil ratio could be adjusted but within 0.40 g to guarantee a uniform powder-like product. After the lithium foil melted, the AlF<sub>3</sub> powder and the liquid Li metal were vigorously stirred, and lithium would become increasingly smaller droplets. After the white AlF<sub>3</sub> powder turned to black and lithium small droplets started to wet the powder, heating was stopped and stirring was continued. After cooling down, LAFN powder was obtained. To make an LAFN electrode, the as-obtained LAFN powder was mechanically pressed, using a pellet die (Aldrich) with ~10 metric tons of pressure. Electrode thickness could be controlled through manipulation of the powder weight. All processes were done in a glove box.

## Characterizations

SEM images were taken with a FEI XL30 Sirion scanning electron microscope. For the SEM characterizations on batteries after cycling, the electrodes were first extracted from the coin cells in the glove box and followed by gentle rinse in 1,3-dioxolane (DOL) to remove Li salt residue. XRD patterns were recorded on a PANalytical X'Pert instrument. To protect the highly reactive Li-related compound from the air, the XRD samples were loaded on a glass slide and covered with Kapton tape in the glove box before the XRD measurements. XPS analysis was obtained on an SSI SProbe XPS spectrometer with an Al (K $\alpha$ ) source.

## Electrochemical measurements on symmetric and full cells

To study the Li stripping/plating processes within a symmetric cell configuration, 2032-type coin cells (MTI) were assembled here. The anodes used here were either the abovementioned LAFN electrodes or the Li foils. To prepare LCO cathodes, lithium cobalt oxide power (MTI) was mixed with carbon black (TIMCAL) and polyvinylidene fluoride (MTI) with a mass ratio of 8:1:1, with *N*-methyl-2-pyrrolidone as the solvent. The mass loading for LCO cathodes was ~4.5 mg cm<sup>-2</sup>. To prepare high-areal capacity LTO electrodes, LTO (MTI), polyvinylidene fluoride (MTI), and carbon black (TIMCAL) were mixed in a ratio of 8:1:1, with *N*-methyl-2-pyrrolidone as the solvent. The areal mass loading of LTO electrodes was ~24 mg cm<sup>-2</sup>. All electrodes used had an area of ~1 cm<sup>2</sup>. The LAFN electrodes used for symmetric cell testing and LCO full cell testing were ~400  $\mu$ m thick, offering an areal capacity ~60 mA-hour cm<sup>-2</sup>. The electrolyte used were 1 M lithium hexafluorophosphate (LiPF<sub>6</sub>) in 1:1 ethylene carbonate/diethyl carbonate (BASF Selectilyte LP40), with 10% fluoroethylene carbonate (Novolyte Technologies Inc.) and 1% vinylene carbonate (Novolyte Technologies Inc.) as additives. Celgard 2325 (25- $\mu$ m polypropylene/polyethylene/polypropylene) was used as the separator. The control bare Li cells were assembled using freshly scraped Li foil. Galvanostatic cycling was conducted either on an Arbin 96-channel battery tester or on a LAND 8-channel battery tester. The EIS measurements were carried out on a Biologic VMP3 system.

## SUPPLEMENTARY MATERIALS

Supplementary material for this article is available at <http://advances.sciencemag.org/cgi/content/full/3/9/e1701301/DC1>

fig. S1. N<sub>2</sub> adsorption-desorption isotherm of AlF<sub>3</sub> powder.

fig. S2. Fabrication of LAFN.

fig. S3. Digital photo of 20  $\mu$ l of ethylene carbonate/diethyl carbonate electrolyte dropped onto Li foil and LAFN electrode.

fig. S4. Transmission electron microscopy characterization of pristine LAFN.

fig. S5. Morphology of LAFN after symmetric cell cycling.

fig. S6. Morphology of LAFN after symmetric cell cycling.

fig. S7. Morphology of LAFN after symmetric cell cycling.

fig. S8. Morphology of LAFN after symmetric cell cycling.

fig. S9. Morphology of LAFN after directly plating Li metal onto its surface.

fig. S10. EIS performance of Li foil and LAFN symmetric cells after different cycles.

fig. S11. EIS performance of LAFN symmetric cells after stripping different percentages of capacity from one side to the other.

fig. S12. Enlarged XRD profile of the dotted box in Fig. 3D.

fig. S13. XPS of LAFN.

fig. S14. Voltage profile of Li foil and LAFN symmetric cell during the 1st, 10th, 50th and 100th cycles, with a current density of 1 mA cm<sup>-2</sup>.

fig. S15. Long-term cycling stability of LAFN electrode.

fig. S16. Symmetric cell cycling performance of LAFN under a current density of 3 mA cm<sup>-2</sup>.

fig. S17. Symmetric cell cycling performance of LAFN under a current density of 5 mA cm<sup>-2</sup>.

fig. S18. Voltage plateau comparison.

fig. S19. Symmetric cell cycling performance of LAFN under a current density of 20 mA cm<sup>-2</sup>.

fig. S20. Symmetric cell cycling performance of LAFN under metabolic current densities.

fig. S21. Symmetric cell cycling performance of LAFN under an areal capacity of 3 mA-hour cm<sup>-2</sup>.

fig. S22. Electrochemical performance of LCO/LAFN cells.

fig. S23. Enlarged voltage profile of LCO full cell batteries.

fig. S24. Electrochemical performance of LCO/LAFN cells.

fig. S25. Electrochemical performance of LTO/LAFN cells.

fig. S26. Electrochemical performance of LTO/LAFN cells for CE testing.

## REFERENCES AND NOTES

1. S. Chu, A. Majumdar, Opportunities and challenges for a sustainable energy future. *Nature* **488**, 294–303 (2012).
2. S. Chu, Y. Cui, N. Liu, The path towards sustainable energy. *Nat. Mater.* **16**, 16–22 (2017).
3. X. Ji, L. F. Nazar, Advances in Li-S batteries. *J. Mater. Chem.* **20**, 9821–9826 (2010).
4. M.-K. Song, E. J. Cairns, Y. Zhang, Lithium/sulfur batteries with high specific energy: Old challenges and new opportunities. *Nanoscale* **5**, 2186–2204 (2013).
5. P. G. Bruce, S. A. Freunberger, L. J. Hardwick, J.-M. Tarascon, Li-O<sub>2</sub> and Li-S batteries with high energy storage. *Nat. Mater.* **11**, 19–29 (2012).
6. H. Kim, G. Jeong, Y.-U. Kim, J.-H. Kim, C.-M. Park, H.-J. Sohn, Metallic anodes for next generation secondary batteries. *Chem. Soc. Rev.* **42**, 9011–9034 (2013).
7. D. Lin, Y. Liu, Y. Cui, Reviving the lithium metal anode for high-energy batteries. *Nat. Nanotechnol.* **12**, 194–206 (2017).
8. K. Yan, H.-W. Lee, T. Gao, G. Zheng, H. Yao, H. Wang, Z. Lu, Y. Zhou, Z. Liang, Z. Liu, S. Chu, Y. Cui, Ultrathin two-dimensional atomic crystals as stable interfacial layer for improvement of lithium metal anode. *Nano Lett.* **14**, 6016–6022 (2014).
9. D. Lin, Y. Liu, Z. Liang, H.-W. Lee, J. Sun, H. Wang, K. Yan, J. Xie, Y. Cui, Layered reduced graphene oxide with nanoscale interlayer gaps as a stable host for lithium metal anodes. *Nat. Nanotechnol.* **11**, 626–632 (2016).
10. J. Heine, S. Krüger, C. Hartnig, U. Wietelmann, M. Winter, P. Bieker, Coated lithium powder (CLIP) electrodes for lithium-metal batteries. *Adv. Energy Mater.* **4**, 1300815 (2014).
11. W. Xu, J. Wang, F. Ding, X. Chen, E. Nasybulin, Y. Zhang, J.-G. Zhang, Lithium metal anodes for rechargeable batteries. *Energy Environ. Sci.* **7**, 513–537 (2014).
12. D. Aurbach, Y. Gofer, J. Langzam, The correlation between surface chemistry, surface morphology, and cycling efficiency of lithium electrodes in a few polar aprotic systems. *J. Electrochem. Soc.* **136**, 3198–3205 (1989).
13. W. Li, H. Yao, K. Yan, G. Zheng, Z. Liang, Y.-M. Chiang, Y. Cui, The synergetic effect of lithium polysulfide and lithium nitrate to prevent lithium dendrite growth. *Nat. Commun.* **6**, 7436 (2015).
14. Y. Lu, Z. Tu, L. A. Archer, Stable lithium electrodeposition in liquid and nanoporous solid electrolytes. *Nat. Mater.* **13**, 961–969 (2014).
15. F. Ding, W. Xu, G. L. Graff, J. Zhang, M. L. Sushko, X. Chen, Y. Shao, M. H. Engelhard, Z. Nie, J. Xiao, X. Liu, P. V. Sushko, J. Liu, J.-G. Zhang, Dendrite-free lithium deposition via self-healing electrostatic shield mechanism. *J. Am. Chem. Soc.* **135**, 4450–4456 (2013).
16. J. Qian, W. A. Henderson, W. Xu, P. Bhattacharya, M. Engelhard, O. Borodin, J.-G. Zhang, High rate and stable cycling of lithium metal anode. *Nat. Commun.* **6**, 6362 (2015).
17. L. Suo, Y.-S. Hu, H. Li, M. Armand, L. Chen, A new class of solvent-in-salt electrolyte for high-energy rechargeable metallic lithium batteries. *Nat. Commun.* **4**, 1481 (2013).
18. A. C. Kozen, C.-F. Lin, A. J. Pearse, M. A. Schroeder, X. Han, L. Hu, S.-B. Lee, G. W. Rubloff, M. Noked, Next-generation lithium metal anode engineering via atomic layer deposition. *ACS Nano* **9**, 5884–5892 (2015).

19. Y. Liu, D. Lin, P. Y. Yuen, K. Liu, J. Xie, R. H. Dauskardt, Y. Cui, An artificial solid electrolyte interphase with high Li-ion conductivity, mechanical strength, and flexibility for stable lithium metal anodes. *Adv. Mater.* **29**, 1605531 (2016).
20. G. Zheng, S. W. Lee, Z. Liang, H.-W. Lee, K. Yan, H. Yao, H. Wang, W. Li, S. Chu, Y. Cui, Interconnected hollow carbon nanospheres for stable lithium metal anodes. *Nat. Nanotechnol.* **9**, 618–623 (2014).
21. K. Liu, A. Pei, H. R. Lee, B. Kong, N. Liu, D. Lin, Y. Liu, C. Liu, P.-c. Hsu, Z. Bao, Y. Cui, Lithium metal anodes with an adaptive “solid-liquid” interfacial protective layer. *J. Am. Chem. Soc.* **139**, 4815–4820 (2017).
22. W. Liu, W. Li, D. Zhuo, G. Zheng, Z. Lu, K. Liu, Y. Cui, Core-shell nanoparticle coating as an interfacial layer for dendrite-free lithium metal anodes. *ACS Cent. Sci.* **3**, 135–140 (2017).
23. G. Zheng, C. Wang, A. Pei, J. Lopez, F. Shi, Z. Chen, A. D. Sendek, H.-W. Lee, Z. Lu, H. Schneider, M. M. Safont-Sempere, S. Chu, Z. Bao, Y. Cui, High-performance lithium metal negative electrode with a soft and flowable polymer coating. *ACS Energy Lett.* **1**, 1247–1255 (2016).
24. H. Wang, M. Matsui, H. Kuwata, H. Sonoki, Y. Matsuda, X. Shang, Y. Takeda, O. Yamamoto, N. Imanishi, A reversible dendrite-free high-areal-capacity lithium metal electrode. *Nat. Commun.* **8**, 15106 (2017).
25. M.-H. Ryou, D. J. Lee, J.-N. Lee, Y. M. Lee, J.-K. Park, J. W. Choi, Excellent cycle life of lithium-metal anodes in lithium-ion batteries with mussel-inspired polydopamine-coated separators. *Adv. Energy Mater.* **2**, 645–650 (2012).
26. D. Lin, D. Zhuo, Y. Liu, Y. Cui, All-integrated bifunctional separator for Li dendrite detection via novel solution synthesis of a thermostable polyimide separator. *J. Am. Chem. Soc.* **138**, 11044–11050 (2016).
27. K. Liu, D. Zhuo, H.-W. Lee, W. Liu, D. Lin, Y. Lu, Y. Cui, Extending the life of lithium-based rechargeable batteries by reaction of lithium dendrites with a novel silica nanoparticle sandwiched separator. *Adv. Mater.* **29**, 1603987 (2017).
28. X. Ji, D.-Y. Liu, D. G. Prendiville, Y. Zhang, X. Liu, G. D. Stucky, Spatially heterogeneous carbon-fiber papers as surface dendrite-free current collectors for lithium deposition. *Nano Today* **7**, 10–20 (2012).
29. C.-P. Yang, Y.-X. Yin, S.-F. Zhang, N.-W. Li, Y.-G. Guo, Accommodating lithium into 3D current collectors with a submicron skeleton towards long-life lithium metal anodes. *Nat. Commun.* **6**, 8058 (2015).
30. X.-B. Cheng, H.-J. Peng, J.-Q. Huang, F. Wei, Q. Zhang, Dendrite-free nanostructured anode: Entrapment of lithium in a 3D fibrous matrix for ultra-stable lithium-sulfur batteries. *Small* **10**, 4257–4263 (2014).
31. K. Yan, Z. Lu, H.-W. Lee, F. Xiong, P.-C. Hsu, Y. Li, J. Zhao, S. Chu, Y. Cui, Selective deposition and stable encapsulation of lithium through heterogeneous seeded growth. *Nat. Energy* **1**, 16010 (2016).
32. Y. Liu, D. Lin, Z. Liang, J. Zhao, K. Yan, Y. Cui, Lithium-coated polymeric matrix as a minimum volume-change and dendrite-free lithium metal anode. *Nat. Commun.* **7**, 10992 (2016).
33. Z. Liang, D. Lin, J. Zhao, Z. Lu, Y. Liu, C. Liu, Y. Lu, H. Wang, K. Yan, X. Tao, Y. Cui, Composite lithium metal anode by melt infusion of lithium into a 3D conducting scaffold with lithiophilic coating. *Proc. Natl. Acad. Sci. U.S.A.* **113**, 2862–2867 (2016).
34. D. Lin, J. Zhao, J. Sun, H. Yao, Y. Liu, K. Yan, Y. Cui, Three-dimensional stable lithium metal anode with nanoscale lithium islands embedded in ionically conductive solid matrix. *Proc. Natl. Acad. Sci. U.S.A.* **114**, 4613–4618 (2017).
35. M. H. F. Sluiter, Y. Watanabe, D. de Fontaine, Y. Kawazoe, First-principles calculation of the pressure dependence of phase equilibria in the Al-Li system. *Phys. Rev. B* **53**, 6137–6151 (1996).
36. Z.-i. Takehara, Future prospects of the lithium metal anode. *J. Power Sources* **68**, 82–86 (1997).
37. S. Shiraishi, K. Kanamura, Z.-i. Takehara, Surface condition changes in lithium metal deposited in nonaqueous electrolyte containing HF by dissolution-deposition cycles. *J. Electrochem. Soc.* **146**, 1633–1639 (1999).
38. Q.-C. Liu, J.-J. Xu, S. Yuan, Z.-W. Chang, D. Xu, Y.-B. Yin, L. Li, H.-X. Zhong, Y.-S. Jiang, J.-M. Yan, X.-B. Zhang, Artificial protection film on lithium metal anode toward long-cycle-life lithium-oxygen batteries. *Adv. Mater.* **27**, 5241–5247 (2015).
39. X.-Q. Zhang, X.-B. Cheng, X. Chen, C. Yan, Q. Zhang, Fluoroethylene carbonate additives to render uniform Li deposits in lithium metal batteries. *Adv. Funct. Mater.* **27**, 1605989 (2017).
40. S. Choudhury, L. A. Archer, Lithium fluoride additives for stable cycling of lithium batteries at high current densities. *Adv. Electron. Mater.* **2**, 1500246 (2016).
41. D. Lin, Y. Liu, W. Chen, G. Zhou, K. Liu, B. Dunn, Y. Cui, Conformal lithium fluoride protection layer on three-dimensional lithium by nonhazardous gaseous reagent freon. *Nano Lett.* **17**, 3731–3737 (2017).
42. M. D. Tikekar, S. Choudhury, Z. Tu, L. A. Archer, Design principles for electrolytes and interfaces for stable lithium-metal batteries. *Nat. Energy* **1**, 16114 (2016).

#### Acknowledgments

**Funding:** Y.C. acknowledges the support from the Assistant Secretary for Energy Efficiency and Renewable Energy, Office of Vehicle Technologies of the U.S. Department of Energy under the Battery Materials Research Program and Battery 500 Consortium. **Author contributions:** H.W. and Y.C. conceived the concept and designed the experiments. D.L. helped set experiment procedures. H.W. performed the materials synthesis. H.W., D.L., Y. Liu, and Y. Li conducted the characterizations. H.W. performed the electrochemical measurement. H.W. and D.L. fabricated the LCO and LTO full cell batteries. H.W. and Y.C. co-wrote the paper. All authors discussed the results and commented on the manuscript. **Competing interests:** The authors declare that they have no competing interests. **Data and materials availability:** All data needed to evaluate the conclusions in the paper are present in the paper and/or the Supplementary Materials. Additional data related to this paper may be requested from the authors.

Submitted 23 April 2017

Accepted 7 August 2017

Published 8 September 2017

10.1126/sciadv.1701301

**Citation:** H. Wang, D. Lin, Y. Liu, Y. Li, Y. Cui, Ultrahigh-current density anodes with interconnected Li metal reservoir through overlithiation of mesoporous AlF<sub>3</sub> framework. *Sci. Adv.* **3**, e1701301 (2017).

## Ultrahigh-current density anodes with interconnected Li metal reservoir through overlithiation of mesoporous AlF<sub>3</sub> framework

Hansen Wang, Dingchang Lin, Yayuan Liu, Yuzhang Li and Yi Cui

*Sci Adv* 3 (9), e1701301.  
DOI: 10.1126/sciadv.1701301

ARTICLE TOOLS	<a href="http://advances.sciencemag.org/content/3/9/e1701301">http://advances.sciencemag.org/content/3/9/e1701301</a>
SUPPLEMENTARY MATERIALS	<a href="http://advances.sciencemag.org/content/suppl/2017/09/01/3.9.e1701301.DC1">http://advances.sciencemag.org/content/suppl/2017/09/01/3.9.e1701301.DC1</a>
REFERENCES	This article cites 42 articles, 4 of which you can access for free <a href="http://advances.sciencemag.org/content/3/9/e1701301#BIBL">http://advances.sciencemag.org/content/3/9/e1701301#BIBL</a>
PERMISSIONS	<a href="http://www.sciencemag.org/help/reprints-and-permissions">http://www.sciencemag.org/help/reprints-and-permissions</a>

Use of this article is subject to the [Terms of Service](#)

---

*Science Advances* (ISSN 2375-2548) is published by the American Association for the Advancement of Science, 1200 New York Avenue NW, Washington, DC 20005. 2017 © The Authors, some rights reserved; exclusive licensee American Association for the Advancement of Science. No claim to original U.S. Government Works. The title *Science Advances* is a registered trademark of AAAS.